

Remote Sensing and Modeling of Coherent Structures in River and Estuarine Flows

Andrew T. Jessup
Applied Physics Laboratory
University of Washington
Seattle, WA 98195-5640
phone: (206) 685-2609 fax: (206) 543-6785 email: jessup@apl.washington.edu

Robert L. Street
Department of Civil and Environmental Engineering
Stanford University
Stanford, CA 94305-4020
phone: (650) 723-4969 fax: (650) 725-9720 e-mail: street@stanford.edu

Stephen G. Monismith
Department of Civil and Environmental Engineering
Stanford University
Stanford, CA 94305-4020
phone: (650) 723-4764 fax: (650) 723-3921 email: monismith@stanford.edu

Alexander R. Horner-Devine
Department of Civil and Environmental Engineering
University of Washington
Seattle, WA 98195-2700
Phone: (206) 685-3032 fax: (206) 685-9185 email: arhd@u.washington.edu

Award Numbers: N00014-05-1-0485 (MURI), N00014-07-1-0898 (DURIP)

LONG-TERM GOALS

The long-term goals of this research are to combine state-of-the-art remote sensing and *in situ* measurements with advanced numerical modeling (a) to characterize coherent structures in river and estuarine flows and (b) to determine the extent to which their remotely sensed signatures can be used to initialize and guide predictive models.

OBJECTIVES

Coherent structures are generated by the interaction of the flow with bathymetric and coastline features. These coherent structures produce surface signatures that can be detected and quantified using remote sensing techniques. Furthermore, a number of relationships between coherent structures and flow characteristics have been suggested that have the potential to allow flow parameters (e.g. mean velocity, bottom roughness, shear, and turbidity) to be inferred from remote measurements. The objectives are to test the following four hypotheses:

Report Documentation Page				Form Approved OMB No. 0704-0188	
Public reporting burden for the collection of information is estimated to average 1 hour per response, including the time for reviewing instructions, searching existing data sources, gathering and maintaining the data needed, and completing and reviewing the collection of information. Send comments regarding this burden estimate or any other aspect of this collection of information, including suggestions for reducing this burden, to Washington Headquarters Services, Directorate for Information Operations and Reports, 1215 Jefferson Davis Highway, Suite 1204, Arlington VA 22202-4302. Respondents should be aware that notwithstanding any other provision of law, no person shall be subject to a penalty for failing to comply with a collection of information if it does not display a currently valid OMB control number.					
1. REPORT DATE 2009		2. REPORT TYPE		3. DATES COVERED 00-00-2009 to 00-00-2009	
4. TITLE AND SUBTITLE Remote Sensing and Modeling of Coherent Structures in River and Estuarine Flows				5a. CONTRACT NUMBER	
				5b. GRANT NUMBER	
				5c. PROGRAM ELEMENT NUMBER	
6. AUTHOR(S)				5d. PROJECT NUMBER	
				5e. TASK NUMBER	
				5f. WORK UNIT NUMBER	
7. PERFORMING ORGANIZATION NAME(S) AND ADDRESS(ES) University of Washington, Applied Physics Laboratory, Seattle, WA, 98195-5640				8. PERFORMING ORGANIZATION REPORT NUMBER	
9. SPONSORING/MONITORING AGENCY NAME(S) AND ADDRESS(ES)				10. SPONSOR/MONITOR'S ACRONYM(S)	
				11. SPONSOR/MONITOR'S REPORT NUMBER(S)	
12. DISTRIBUTION/AVAILABILITY STATEMENT Approved for public release; distribution unlimited					
13. SUPPLEMENTARY NOTES					
14. ABSTRACT					
15. SUBJECT TERMS					
16. SECURITY CLASSIFICATION OF:			17. LIMITATION OF ABSTRACT Same as Report (SAR)	18. NUMBER OF PAGES 28	19a. NAME OF RESPONSIBLE PERSON
a. REPORT unclassified	b. ABSTRACT unclassified	c. THIS PAGE unclassified			

1. Flow parameters can be inferred from remotely sensed signatures of coherent structures.
2. Numerical models can be constrained with these inferred parameters.
3. The effect of stratification on the strength of coherent structures can be used to detect the presence or absence of stratification and the location of the fresh/salt water interface.
4. Numerical and field experiments can be used together to predict, interpret, characterize, and understand coherent structures.

APPROACH

The key to this project is an interactive process that blends sophisticated remote sensing, in-situ measurements, and numerical simulation. Our approach is to conduct closely coupled field and numerical model experiments to test the hypotheses listed above. The plan includes two major field experiments with both *in situ* and remote sensing measurements – the first occurred in 2006 (Year 2) and the second occurred in 2009 (Year 5), and was planned using results from the pilot experiment which took place in September 2008. A preliminary experiment was conducted in 2005 (Year 1) to aid in the design of the major field efforts. The research involves four main areas - (1) *in situ* measurements, (2) remote sensing, (3) modeling, and (4) physics and classification of coherent structures. The *in situ* field measurements are used to characterize the overall flow field to investigate the generation of coherent structures at specific sites, and initially, to provide boundary inputs for the numerical models. The surface signatures of coherent structures in the same region are detected using remote sensing techniques and compared with the *in situ* and model results. Results from the *in situ* field observations, remote sensing, and numerical model runs will be synthesized into a classification scheme that includes all observed coherent structures. Predictive scaling relationships will be developed in order to generalize the results from this study to other systems. The result of this integrated approach will be a thorough investigation of the mechanisms and evolution of coherent structures in rivers and estuaries in order to link their surface expressions to subsurface flow features.

The project participants have been organized into teams identified by the main areas of interest listed above: *Remote Sensing*: A. Jessup, C. Chickadel (APL-UW), W. Plant (APL-UW); *Modeling*: R. Street and O. Fringer (Stanford); *In situ Measurements*: S. Monismith and D. Fong (Stanford); *Physics and Classification*: A. Horner-Devine and S. Talke (UW).

WORK COMPLETED IN FY09

The focus of this reporting period was:

- analysis of the data from the 2008 pilot experiment
- ongoing numerical modeling effort
- further analysis of exploratory laboratory experiment
- Second and final major field experiment in 2009

RESULTS

This report will focus on the following areas (by lettered sections with lettered and numbered figures):

- A: 2009 Field Experiment Overview
- B: Thermal IR imaging (barge and airborne) (UW, APL)
- C: In Situ Measurements of Estuarine Dynamics (Stanford)
- D: Physics and Classification of Coherent Structures – lab expt. (UW, Civil and Env. Eng.)
- E: Numerical Modeling (Stanford)
- F: Microwave Remote Sensing (UW, APL)

A: 2009 FIELD EXPERIMENT OVERVIEW

The final major field experiment of the project was conducted from 8-25 Sep 2009 on the Snohomish River in Everett, WA. The UW research barge R/V Henderson was used to acquire infrared imagery and near surface turbulence measurements. The left photograph in Figure A1 shows the instrument boom (raised position) attached to the bow of the Henderson. The front of the boom has a sub-surface frame with an array of velocity sensors and the tower with an infrared camera. The Henderson was equipped with movable pilings, or spuds, which provided rapid mobility that allowed us to make measurements routinely on both flood and ebb tides. The spuds also provided exceptional stability for the turbulence measurements. The right photograph in Figure A1 shows the Helikite platform used to provide large area infrared imagery.

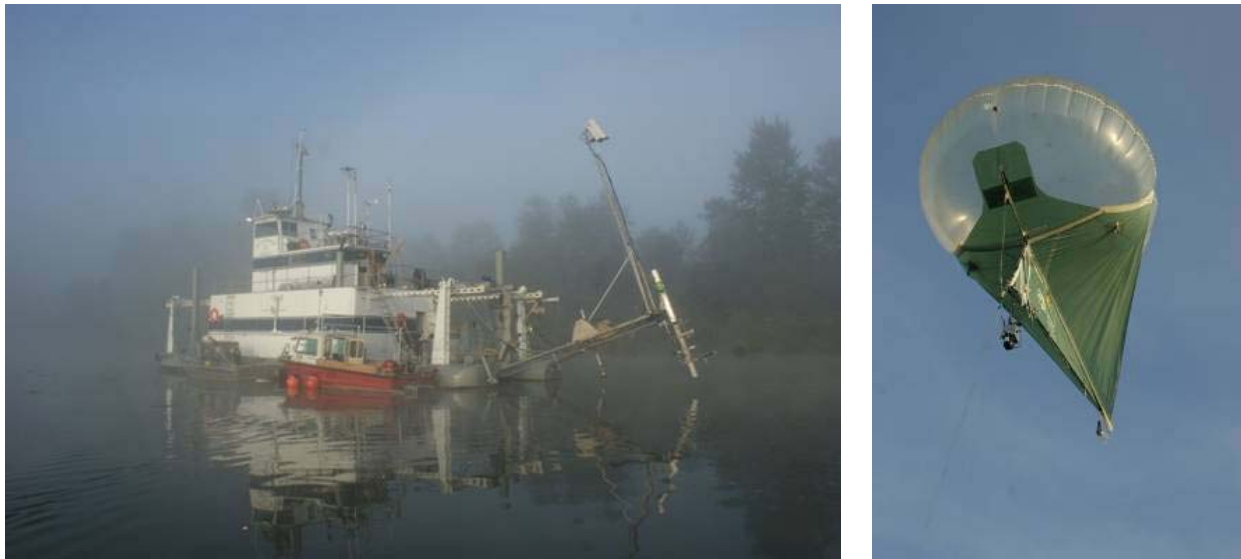


Figure A1. (left) Photograph of UW research barge R/V Henderson showing instrument boom used for infrared imagery and subsurface turbulence measurements. (right) Photograph of Helikite used for large field-of-view infrared imagery.

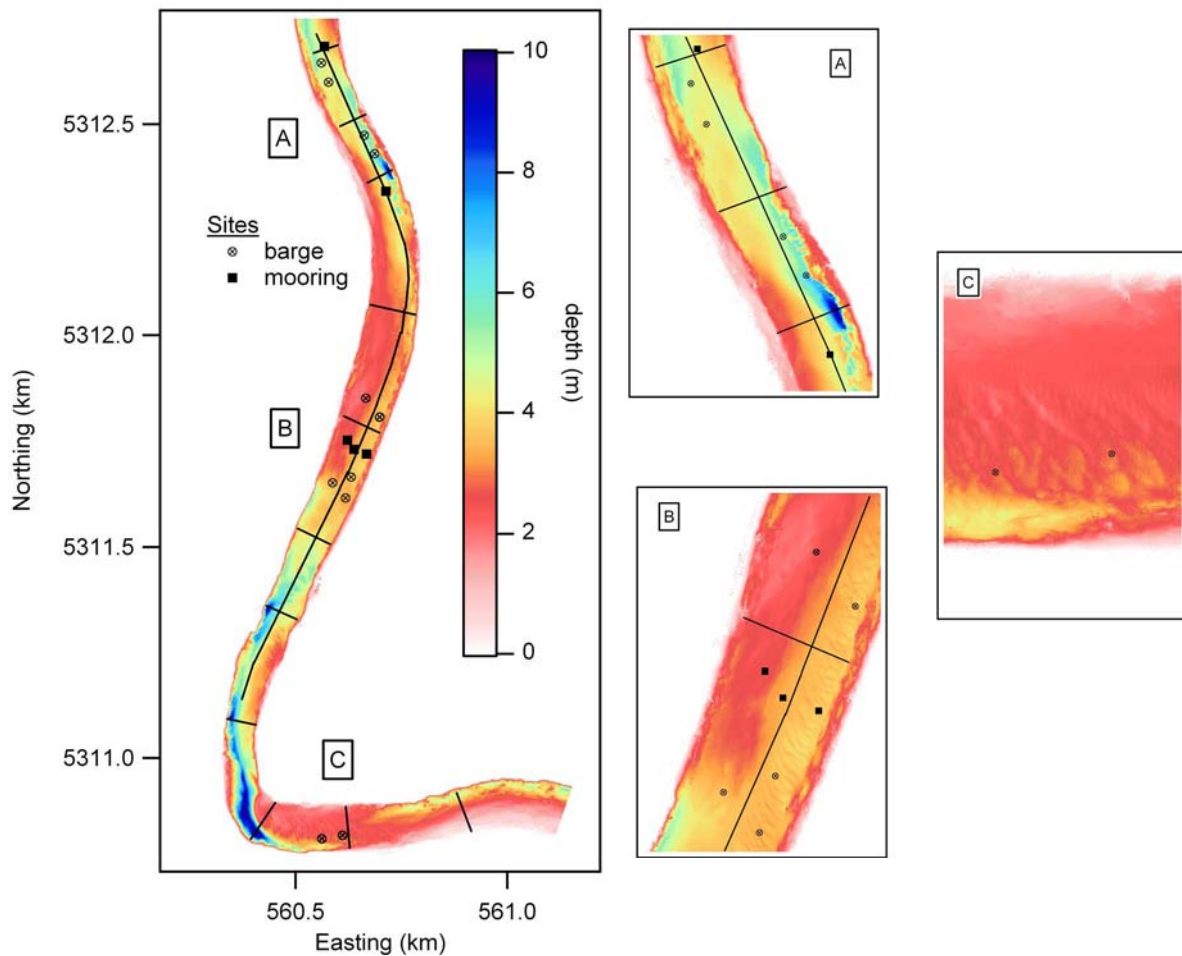


Figure A2. 2009 Study Region. (left) Overview and (right) Sites A-C in detail. The line along the channel marks the path of REMUS while cross channel lines indicate ADCP/CTD transect paths.

The measurements were made at three sites within a 2.5 km stretch of the river located approximately 15 km upstream from the mouth. The distance upstream was chosen in order to minimize the influence of stratification. The specific stretch of river was chosen because of the proximity of a variety of bathymetric features of interest. Figure A2 shows an overview of the bathymetry of the study area and details of the individual sites designated as A-C. The figure shows the location of the barge at each site as well as the moorings, which were located at sites A and B only.

B: THERMAL IR IMAGING

A previous one-week pilot field experiment in September 2008 on the main channel Snohomish River informed our intensive three-week experiment on the same stretch of the Snohomish River, successfully completed in September 2009. The thermal imagery was gathered from a nested suite of imaging platforms to capture infrared (IR) signatures of river flow at scales from millimeters to tens of meters. Using the data gathered in both 2008 and 2009, we are focusing our investigation on the spatial and temporal development of observable surface coherent structures and how they relate to the

underlying flow conditions (esp. depth and bottom roughness). During FY2009 our research has specifically included:

1. Analysis of surface thermal images for surface turbulent (boil) properties, and
2. Development and testing of a 2D PIV algorithm for IR video data.

Surface turbulence characteristics

Estuarine and river turbulence can be enhanced by flow over bathymetric features and obstructions, rough bottoms, or strongly sheared flow, while density stratification due to salt wedge intrusion can suppress it. Our hypothesis remains that we can deduce these effects from IR remote sensing data. Our recent set of experiments in the Snohomish River near its mouth have documented a range of rapidly evolving structures in infrared video made evident by disruption of the cool skin layer by turbulent straining and upwelling. The novel aspect of this data is its ability to directly reveal spatial scales of turbulence in a snapshot without having to rely on advection of the turbulent field past a sensor.

In our analysis, we have quantified the spatial structure of the surface temperature patterns over the course of a flooding tide through two-dimensional Fourier analysis. As shown in the example in Figure B1, the river flow increases from zero velocity to a stable flow of ~ 0.6 m/s while the surface temperature structure patterns quickly develop from short length-scale, wind-driven patterns at low flow speeds patterns consistent with the theorized $k^{-5/3}$ Kolmogorov cascade present in fully turbulent flow (lower panels). Comparisons of this data with in situ estimates of turbulence spectra are underway, and we hope to be able to use the thermal turbulence spectra to provide a direct estimate of turbulent energy and dissipation of the flow. In the interim, our analysis is continued by constructing a simple metric to capture the development of surface turbulence as ratio of larger-scale (> 1 m) energy to the smaller-scale (< 1 m) energy. This metric, plotted in Figure B2, tracks the increasing surface turbulent signature strength as river flow increases, indicated by the relative increase in longer length-scales in the surface signatures. We will continue our analysis by testing this metric with our 2009 data, using it as a proxy for turbulent strength in river flow over variable bottom conditions.

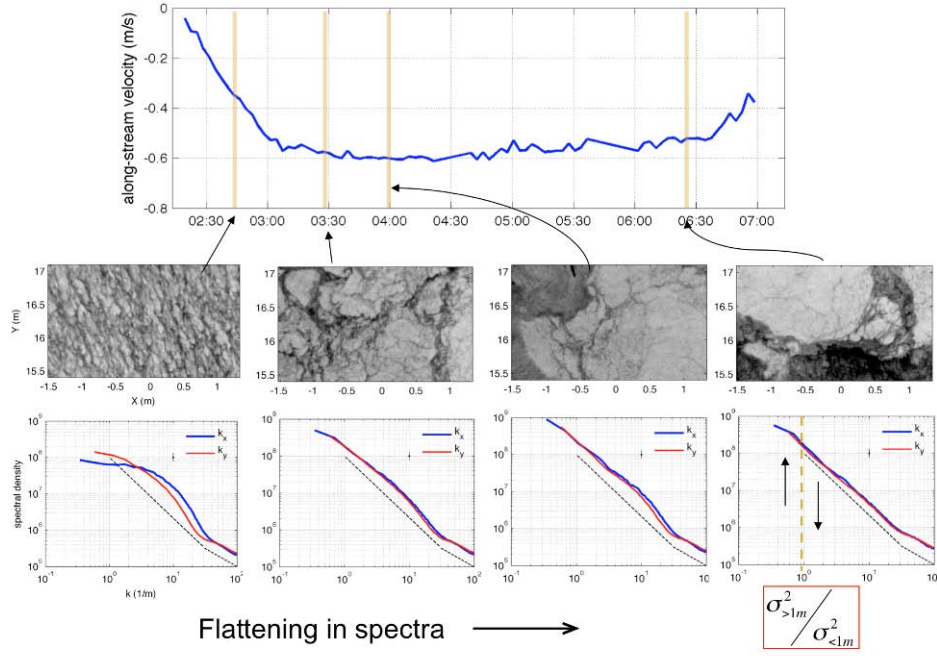


Figure B1. (top panel) Alongstream flow of the Snohomish River during an ebbing tide in 2008. (middle panels) Examples of surface temperature patterns during development of river flow changing from small wind driven structures to flow derived turbulent boils, and (bottom panels) associated wavenumber spectra of the thermal images. The dashed lines indicate the expected $k^{-5/3}$ turbulence cascade transitioning to the k^{-1} thermal dissipation, at high wavenumbers.

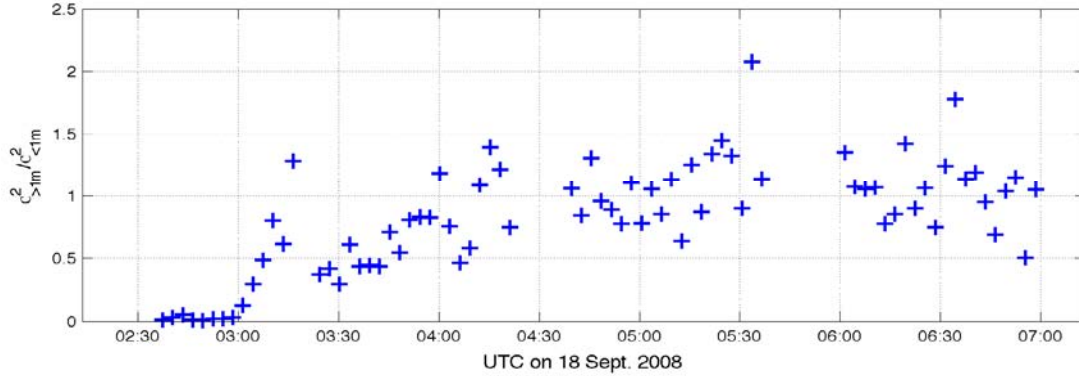


Figure B2. Time series of the ratio of log to short wavelength energy in thermal imagery, (see Figure B1). The increase in the metric coincides with the increase in larger-scale surface turbulence (boils) in the river.

2D Infrared PIV

Previously, a one-dimensional (1D) particle image velocimetry (PIV) technique was validated against 2006 field data. A custom 2D PIV technique has been developed and implemented on the 2008 data for application to our 2009 experiment. The technique is based on phase correlation and resolves the

horizontal velocity field with a grid spacing (6.25cm) fine enough to resolve turbulent river flow. The example shown in Figure B3 details the PIV velocity field associated with a passing boil and the associated divergence calculated from the PIV results. The divergence associated with the center of the boil is consistent with a region of upwelling at the surface, thus leading to the warm boil pattern, while the background flow streams around the boil. Measurements from a collocated acoustic Doppler velocimeter (ADV) agree well with PIV estimates (Figure B4), though noise in the ADV measurement due to its orientation prevents a hard quantitative comparison. However, by using conservation of mass it is possible to estimate the vertical component of velocity due to divergence or convergence at the surface. Our estimate of the vertical velocity in this example (Figure B4) compares well with the measured velocity. Future analysis will continue validation of the PIV algorithm against in situ measurements. In future analysis we plan to estimate relevant turbulent properties (e.g. turbulent kinetic energy, Reynolds stress, and dissipation) from PIV velocity estimates and use them in conjunction with in situ estimates to better understand the turbulent flow properties of the river. Understanding the turbulent properties in river and estuarine flow is also critical to understanding mixing and important as input to hydrodynamic models.

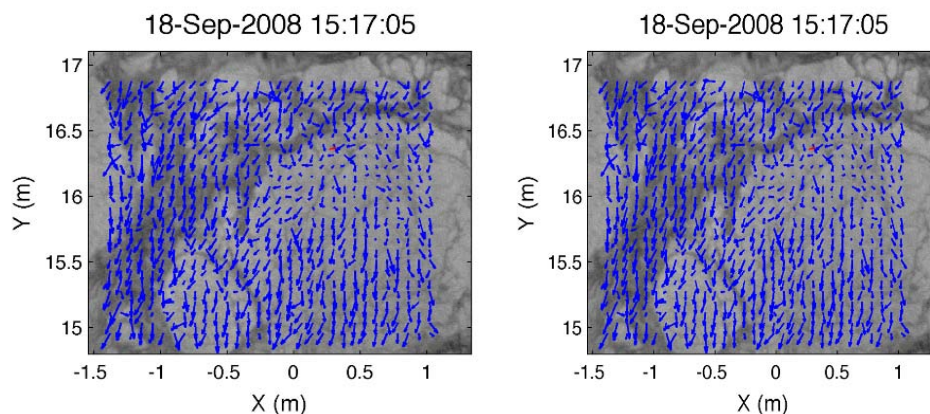


Figure B3. (left) Snapshot of PIV estimate flow vectors associated with an erupting boil - the large bright, warm feature. (right) Calculated divergence pattern demonstrating divergences at the boil center. The circle indicates the location of a submerged ADV.

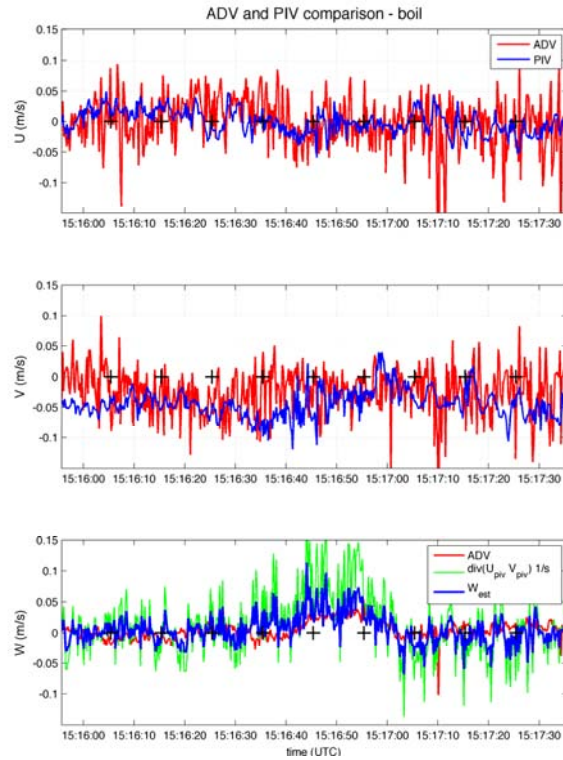


Figure B4. *PIV and ADV comparisons of the cross-stream (top panel) and alongstream (middle panel) river flow bracketing the time of the snapshot shown in Figure B3. (bottom) Measured and surface PIV based vertical velocity of the flow associated with the passage of a boil, approximately from 15:16:40 to 15:17:00 UTC. Both measurements show good agreement.*

C: IN-SITU FIELD MEASUREMENTS

During FY2009 our efforts have been focused on further analysis of the data obtained in July 2006 and 2008 as well as preparing for and conducting the in-situ measurements for the second large-scale study in September 2009. The work completed on the 2006 data has been incorporated into one submitted manuscript, presentations at several conferences, and two additional papers in preparation. The 2009 in-situ field measurements were very successful and provide the overall hydrodynamic conditions in which the other measurements took place.

Further analysis of July 2006 data

The active areas of research utilizing the 2006 dataset include further frontogenesis analysis through merging all of the COHSTREX team measurements, a detailed look at vertical mixing and stratification, and a momentum budget analysis. The overall goal of these research themes is to try to better understand the dynamics unique to shallow, macrotidal estuarine systems and systems with large intertidal regions or regions with large tidal amplitude to depth ratios.

We submitted a paper examining the advantages and disadvantages of different methods at capturing frontal dynamics. We focused on the convergence front near Jetty Island by combining all of the

COHSTREX 2006 measurement techniques. We performed qualitative and quantitative comparisons between the in-situ measurements, REMUS autonomous underwater vehicle (AUV) measurements, visual and infrared imagery, and radar remote sensing. The important contributions include direct comparisons of in-situ measurements with several methods that previously only had minimal in-situ verification as well as the successful application of using an AUV outfitted with both an ADCP and a CTD to measure fronts in a narrow, shallow estuary. Ultimately we highlighted the benefits of a multi-modal approach such as that of the COHSTREX team to better understand complex estuarine and riverine dynamics (see *Figure C1*).

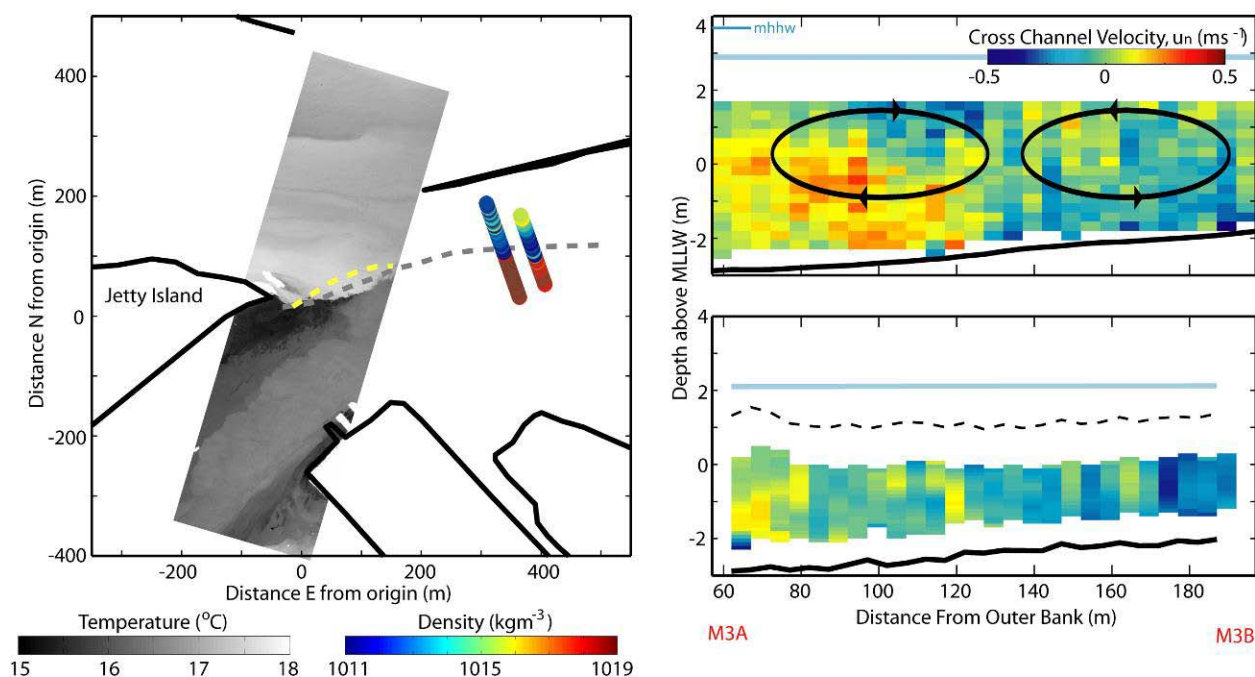


Figure C1. Overlap of various techniques measuring a coherent convergent front.

The map on the left highlights the ability to overlay our broad array of instrumentation to better understand a coherent surface feature, a trapping front. An aerial thermal IR image is overlain with locations of the front determined from the radar (yellow dashed line) and SUNTANS numerical simulations (grey dashed line). Additionally, the density from the boat mounted ADCP (colored circles) and REMUS AUV (colored circles offset to the right) are shown which agree well. The figures on the right show the surface convergent cross channel circulation cells measured by the transecting ADCP (top panel) and REMUS (bottom panel) demonstrating the successful application of utilizing REMUS to obtain cross-frontal circulation patterns. All of these measurements were taken at the same time in the tidal cycle near peak flood currents demonstrating the success and corroboration of these various methods to identify the front.

Due to the large tidal range and shallow depths of this estuary, this comprehensive dataset is a wonderful tool for trying to better understand dynamics in this type of system. Shallow, macrotidal, salt-wedge estuaries are not well understood and further analysis will provide a large contribution to the estuarine hydrodynamics community. To date we have made significant progress on two additional

papers, one examining the overall circulation and mixing in the Snohomish as well as a paper examining the detailed frontogenesis mechanism utilizing all of the techniques discussed in the submitted manuscript. Both address the questions of dynamics in macrotidal systems: the first emphasizes the dynamics unique to macrotidal and salt-wedge estuaries, while the second describes a frontogenesis mechanism that is poorly understood yet likely common in estuaries with large intertidal or shoal regions. Furthermore, we have examined the vertical mixing and stratification in the Snohomish in detail indicating the importance of mixing along the salt-wedge interface rather than bottom-generated mixing. Finally, we have begun analysis on tidally averaged circulation in this system which is different from traditional estuarine circulation in that it contains effects of both the longitudinal density gradient as well as tidal residuals.

Snohomish September 2008 in-situ measurements

The Snohomish September 2008 preliminary experiment was conducted in preparation for the 2009 experiment. Our in-situ contributions included one mooring with near surface and bottom conductivity, temperature, depth sensors (CTD), as well as a bottom mounted acoustic Doppler current profiler (ADCP); boat-mounted ADCP transects; and an ADCP mounted to the barge. The mooring data was analyzed and presented in FY2008. In FY2009, we continued analysis of this dataset completing data processing of the transect data and the barge-mounted ADCP. The transect data demonstrated cross channel variability in the along channel velocity as well as cross channel circulations which were used to inform the barge measurements and the numerical modeling. The Benilov method was applied to remove boat motion from the barge-mounted ADCP which allowed us to successfully compute Reynolds stresses from this platform.

Snohomish September 2009 in-situ measurements

During September 2009 we deployed five moorings and conducted boat transects to provide the hydrodynamic conditions throughout the 2009 experiment. Figure A (see above) shows the local bathymetry and the locations of the barge, moorings, and transect paths. The furthest north mooring is A1, then A2. Site B included B1, B2, and B3 from west to east respectively. Each mooring had a bottom mounted ADCP and CTD, as well as a CTD near the water surface. The mooring locations were chosen to compliment the barge locations as well as to provide measurements at locations with varying bottom roughness ranging from very flat (mooring B1) to large sand waves (mooring B3). Additionally, we conducted transects with a boat-mounted ADCP and CTD in several hour blocks throughout the experimental period overlapping with the barge-mounted measurements. Finally, we also deployed REMUS for two missions running near the center of the channel from mooring A1 to just north of the sharp bend in the river.

The in-situ instrumentation was largely a success with only some loss of data from a couple bottom mounted CTDs that became covered in sand. Figure C2 shows the along channel velocities and Reynolds stresses as well as the density computed from the top and bottom CTDs at one of the moorings (B1). The velocity shows strong tidal influence as we expected with maximum currents just less than 1ms^{-1} . We observe strong neap/spring variability as well as the influence of enhanced river flow during the first two days of the deployment. The stresses also exhibit strong tidal modulation with the highest stresses near the bed during peak spring tide currents. The cross channel velocities (not shown) exhibit secondary circulation in the sense expected due to the local river curvature (towards the outer bank at the surface and towards the inner bank at the bottom). During the month, the system alternates between states, sometimes behaving as a well mixed estuary; sometimes exhibiting strong

stratification; and sometimes acting as an unstratified tidal river. The presence of stratification at times plays a role in the physics as evidenced in the cross channel velocities and strong lateral convergences we observed.

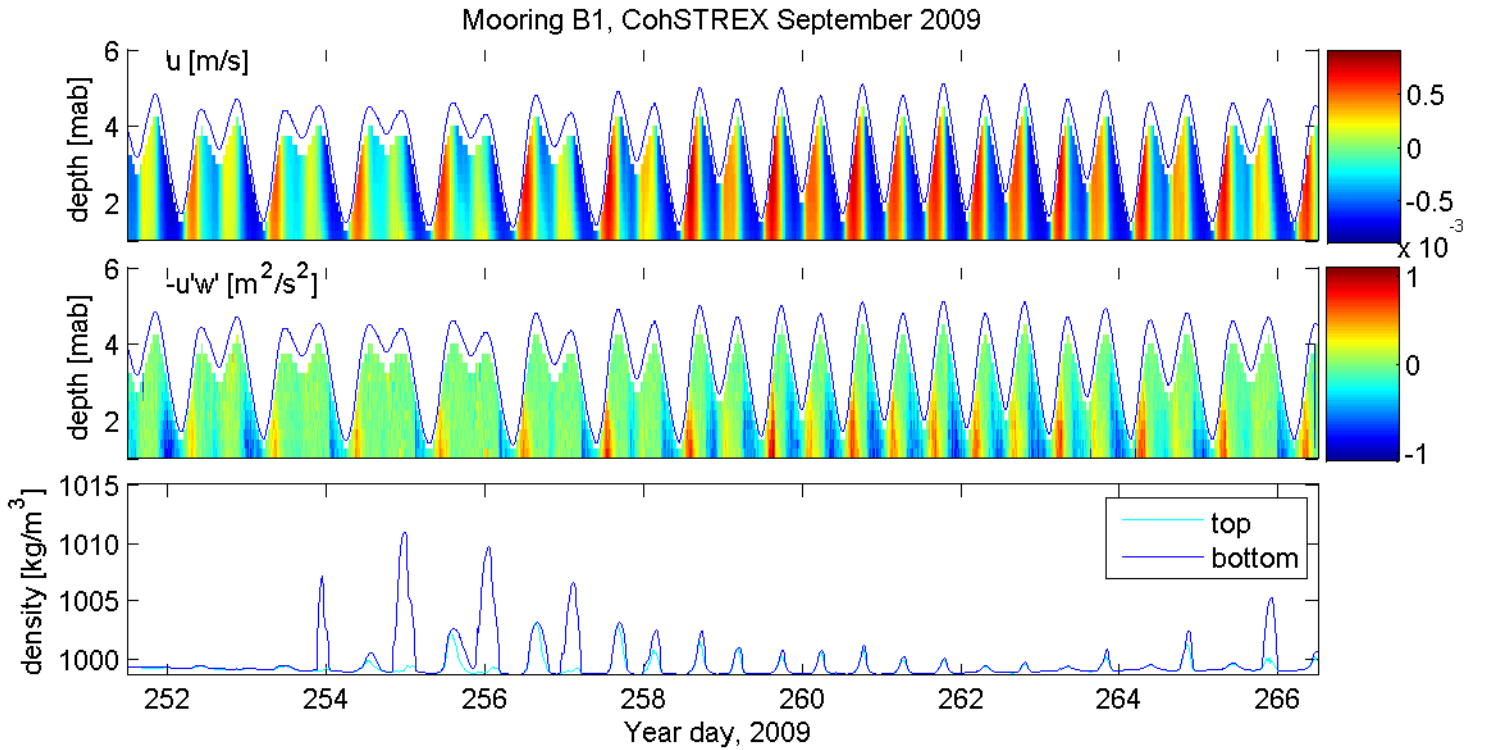


Figure C2. Snohomish 2009 mooring B1 velocity, stress, and stratification. The top panel displays the along channel velocity from the moored ADCP derived via principal component analyses. Positive along channel flows are in the direction of the flooding current (approximately towards the south-west). The middle panel shows the computed along channel Reynolds stresses. The bottom panel shows the top and bottom density derived from the CTDs.

Four of the five moorings were level enough to compute Reynolds stresses which will allow us to connect these measurements with the near surface barge-mounted instrumentation to investigate Reynolds stresses throughout the water column. The stresses also allow us to compute the coefficient of drag, C_d , at each location. Preliminary examination of stresses indicates significant variation depending on the bottom roughness. This information will be very important when interpreting boil generation and propagation from the other instrumentation.

REMUS confirmed the variations in bottom bathymetry at the different sites (see Figure C3). We will be able to use this information as well as the multibeam bathymetry data collected to connect bedforms and roughness with measurements of C_d . Furthermore these REMUS missions tested the vehicle's ability to maneuver in such a narrow, shallow tidal river. As we found in 2006, operating REMUS in this environment poses many difficulties as the acoustics are difficult to optimize and REMUS does not keep its designated course well.

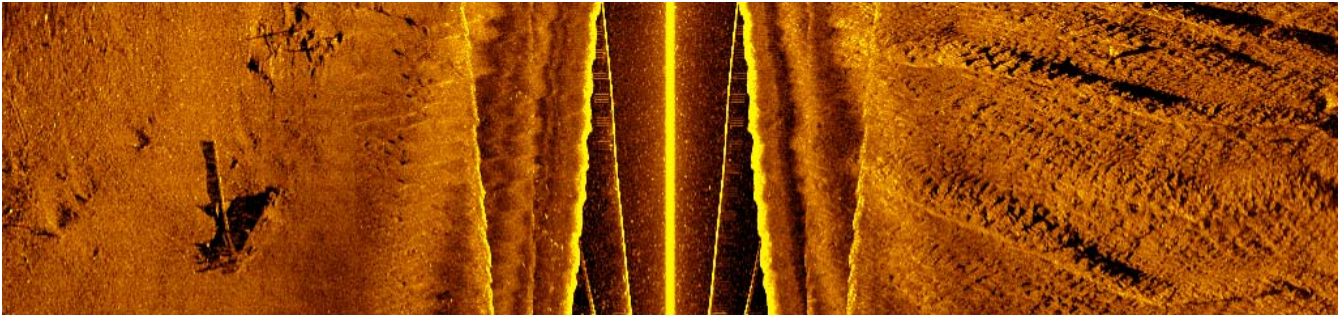


Figure C3. REMUS sidescan sonar image near site B. taken from the center of the channel near. The range on either side of the instrument is 30m. The east bank (right side of image) is dominated by large sand waves while the west bank (left side) is nearly flat with some individual features (submerged logs). This matches well with the multibeam bathymetry data.

Overall the in-situ measurements were a success. We measured both the background hydrodynamic conditions and more detailed measurements that may aid in understanding boil generation and evolution. We plan to continue analysis both on this newly acquired dataset as well as that from 2006 to form a comprehensive view of circulation and mixing in this estuarine system. This will be useful to understanding dynamics in macrotidal systems as well as to continue to use the in-situ measurements to validate the barge-mounted and radar measurements.

D: PHYSICS AND CLASSIFICATION OF COHERENT STRUCTURES

During the year ending September 2009, the “physics and classification of coherent structures” subgroup of the COHSTREX project made significant progress in analyzing coherent structures from the 2006 experiment, focusing on the mechanics of vertical boil propagation, the development of coherent structures in sheared flow, and boiling that occurs due to unstable lee-waves (see below).

In addition, we designed and implemented an array of sub-surface velocity measurements as part of the September 2009 field experiment on the Snohomish River. These measurements, which were co-located with surface infra-red video measurements, are critical for connecting surface expressions of flow and turbulence to in-situ coherent structures. Conditions over the three week experiment were largely calm (few windy periods), ideal for measuring turbulence quantities. Initial results are promising, as described below.

Field Experiment

Four primary objectives drove our in-situ velocity measurements within the IR field of view:

1. To determine the subsurface velocity structure of boils observed in the IR imaging
2. To compare subsurface turbulence statistics with those derived from the IR fields
3. To investigate the distortion of turbulent eddies resulting from the free-surface
4. To determine how differing bottom bathymetry, ranging from relatively smooth to rough (dunes and holes), affects coherent structure expression.

Instruments were mounted on a rigid T-shaped frame, which was mounted to the A-frame on the R/V Henderson (Fig. D1). The R/V Henderson was rotated so that the instrument frame was oriented into the flow for both floods and ebb tides. The instruments sampled far upstream of the vessel wake. The instrument array consisted of four vertically spaced Acoustic Doppler Velocimeters (ADV) positioned 1.5m, 0.7m, 0.4m and 0.05 m from the water surface and two laterally spaced ADVs located 1.1m and 0.6m from the center (Fig. D1). Two Nortek Aquadopp Acoustic Doppler Profilers (ADPs) were mounted to the frame; one mounted 1m below the water surface in an up-looking configuration and the other mounted 0.3m below the water surface in a side-looking configuration. Finally, a downwards looking 1200kHz RDI ADCP was mounted on the A-frame 2.5m behind the ADV/ADP frame.



Figure D1: Henderson in situ instrument array shown close up (left) and in relation to the frame-mounted IR camera (right).

The most significant challenge to making turbulence measurements using ADVs on a floating platform such as the R/V Henderson is ensuring that they are not contaminated by vessel movement (pitch, roll, or vibration) or vibration of the frame relative to the vessel. Vessel movement was operationally eliminated as a result of the new 5000 lb spuds that were installed fore and aft on the Henderson. Although boat wakes during daylight hours still resulted in some platform movement, very little movement occurred during our sampling periods, which were at night. Rigidity of the instrument frame was achieved by adding a series of cross-braced stainless steel stays. Finally, the frame was equipped with a 100hz inertial motion unit (IMU) so that any unwanted vibration was detected and could potentially be removed. Although a narrow band vibration at 7 Hz was observed in the IMU data, no corresponding peak was observed in the velocity data. Other sources of error, such as high levels of detritus in the river, were periodically removed.

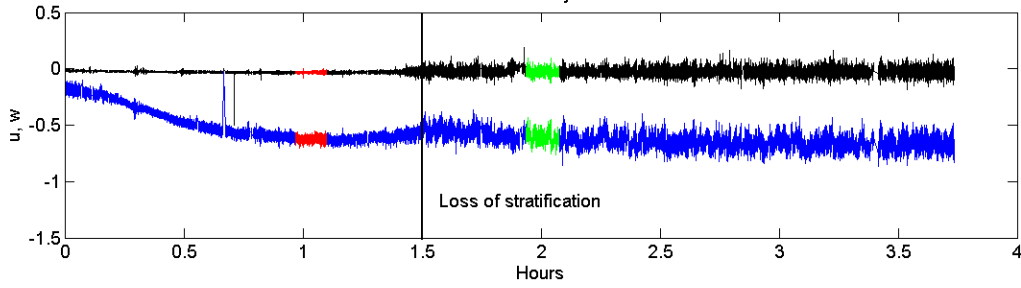


Figure D2: Streamwise (u , blue) and vertical (w , black) velocities from an ADV located 1.5 below the water surface during an ebb tide that was stratified for the first 1.5 hours.

Observations

Although the 2009 experiment was located more than 15 km from the river mouth in a region of the river that was not expected to be stratified, we observed significant stratification during some high tides. The ADV array was located in relatively unstratified, surface water; however, decoupling of the surface flow from the bottom due to stratification had a pronounced effect on the near-surface turbulence.

Figure D2 shows the velocity record from the lowermost ADV (1.5m) during an ebb tide that was stratified for the first 1.5 hours. During the stratified period the flow accelerates to more than 0.6m/s, but the magnitude of turbulent fluctuations is dramatically reduced relative to later in the tide. For comparison, the periods highlighted in red and green have the same along channel velocity, but the mean turbulent kinetic energy is an order of magnitude smaller during the stratified (green) period.

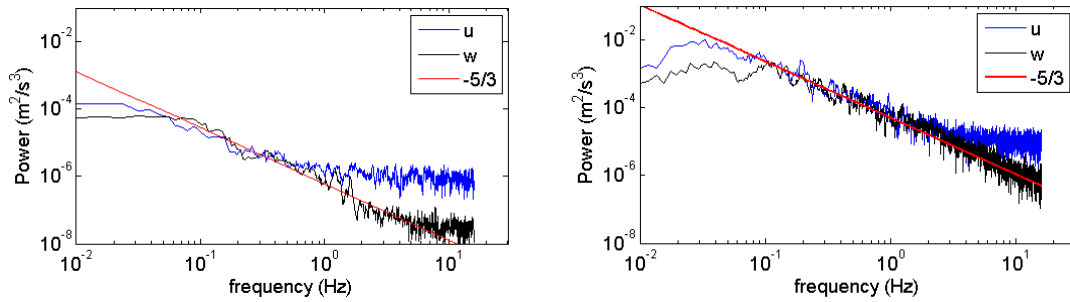


Figure D3: Power spectra for low (left) and high (right) velocity periods. Both spectra show very clear $-5/3$ slopes corresponding to the inertial subrange. The $-5/3$ fits to the data result in estimates of the tke dissipation rate of $\varepsilon = 6 \times 10^{-8}$ W/kg and $\varepsilon = 1.5 \times 10^{-5}$ W/kg for the low (left) and high (right) energy periods, respectively.

Resolution of turbulence scales

In order to confidently address our objectives, it is necessary to resolve a significant range of turbulent motions in low and high flow conditions. Because the ADVs were recorded in real-time, they could be tuned constantly so that they were sampling in a mode that was optimized to the changing flow conditions. As a result, we were able to resolve turbulent motions for very slow, low energy flows ($u =$

0.16m/s, TKE dissipation = 6×10^{-8} W/kg) and faster, more energetic flows ($u=0.6$ m/s TKE dissipation = 1.5×10^{-5} W/kg). Power spectra for these two cases are shown in Figure D3. Both cases display very clear -5/3 slopes, indicating that we resolve the inertial subrange over more than two orders of magnitude, even in very low energy conditions.

Coherent Structures Analysis from 2006

During this year we have made significant progress in understanding how coherent structures are produced in sheared, separated flow (Talke & Horner-Devine, JGR accepted). As an example, we show below turbulence statistics about 7 m downstream of a steep, 4 m tall sill (Fig. D4). Production of turbulence occurs in the highly sheared upper water column, leading to large turbulent kinetic energy (velocity variance), and is not connected to the bed. Coherent structures are observed to impinge the surface in both backscatter and along beam velocity (Talke & Horner-Devine, JGR accepted). Similar analysis will be done with the 2009 data set, with the probable difference that turbulence (i.e., coherent structures) will be produced near the bed due to the smaller bathymetry at the experiment locations.

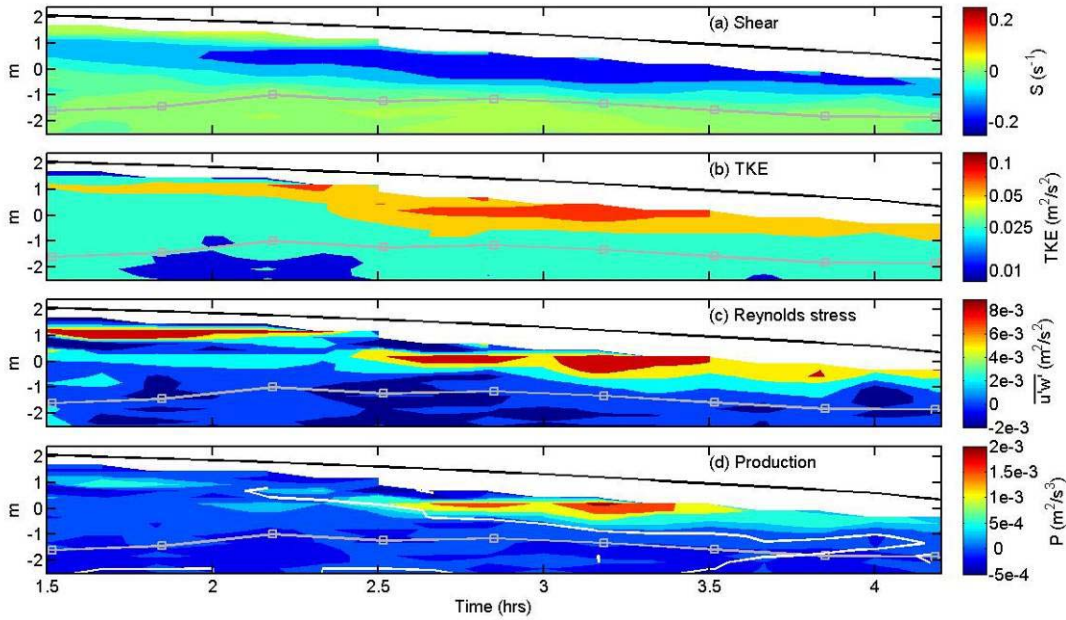


Fig. D4: Estimates of shear, turbulent kinetic energy (TKE), Reynolds stress, and Production of TKE from an ebb tide on July 21st, 2006.

Internal Lee waves

Motivated by observations of frontal features observed in infra-red imaging of flow over the 2006 sill, we have investigated a second mechanism for the formation of surface boils—namely, an internal hydraulic jump that occurs because of an unstable internal (lee) wave during highly stratified conditions (Fig. D5). We have developed a novel way of using backscatter to image the internal wave. Combined with the surface IR measurements and our analysis of velocity data, the resulting data set provides a unique, quasi 3D view of unstable lee waves (as described below).

Surface maps of water temperature from a lift-mounted long-wave infrared camera indicate the formation of a convergence front just downstream of the sill crest during the early ebb. Over time, this front moves downstream, and cool bottom water begins to boil through the water surface on its downstream side. These movements are simultaneously captured by an in-situ, upward facing ADCP and a high resolution, single beam echosounder. Upwelling, vertical velocities (~ 10 cm/s) correspond to the boiling action observed at the surface. At the convergence, flow is angled strongly downward. Internal density interfaces are observable in in-situ, elevated acoustic backscatter measurements. These interfaces deform as the surface front passes over the sensor (solid line in the upper panels of Fig. D5). We reconstruct the x, y, z coordinates of the deforming density interface over time, using the property that the acoustic beams have independent trajectories. The resulting time series shows an unstable internal wave interface that advects downstream and changes shape over time. For example, a trough is observed at 53.4 minutes, while a steep wave face is observed at 54 minutes (note that colorbar indicates vertical height of the density interface). Surface IR shows lateral (along-sill) instability in the wave, with a length-scale of 20-30 m. As upstream flow accelerates, the lee wave amplitude increases and the wave face steepens, ultimately resulting in the release of the wave downstream (which is tracked by the surface IR). Downstream release first occurs on the channel side of the sill, and propagates towards the shore with speeds of up to 30 cm/s. Further evidence of lateral instability is found in transect data, which shows transverse variations in internal density interfaces. Several sequences of lee-wave formation and release occur consecutively. The resulting picture provides insights into how the lee-wave evolution of flow over real bathymetry is influenced by lateral variability.

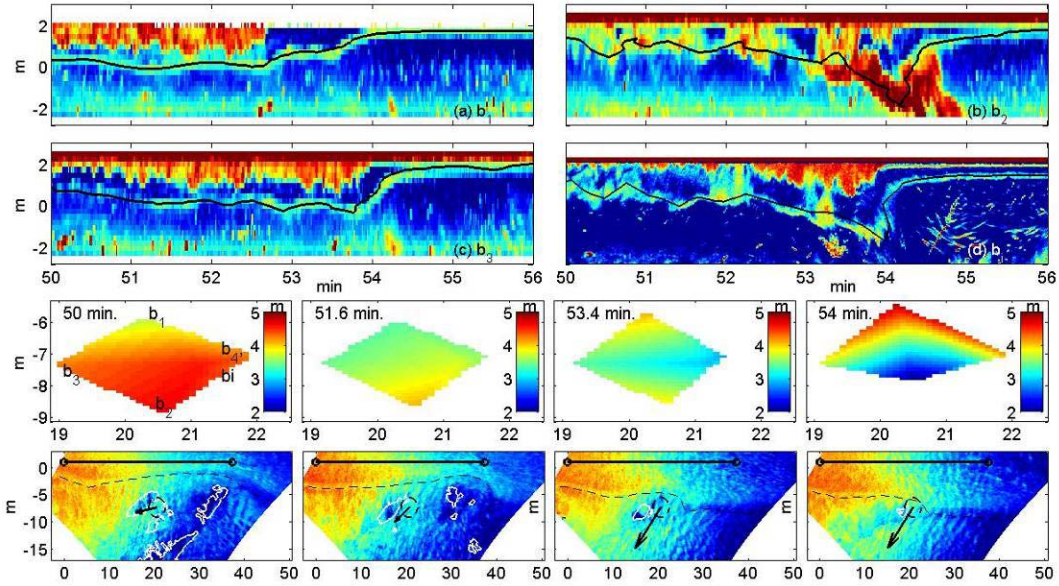


Fig. D5: Observations of backscatter from 4 ADCP beams (upper 4 panels), and the progression of an in-situ density interface constructed from those beams (labeled 50 min, 51.6 min, 53.4 min, and 54 min). Note that the colorbar gives the vertical height of the interface, and the x and y axes are the sill parallel and sill-perpendicular directions. The bottom four panels show the simultaneous evolution of a front observed in IR video. Patches of upwelling are shown in white and the ADCP flow vector emanates from the in-situ tripod location. The frontal feature is depicted by a dashed line, while the solid black line shows the location of the sill crest.

E: NUMERICAL MODELING

Estuary-scale simulations with SUNTANS

During the past year we have focused on understanding the variability of turbulent mixing in the Snohomish River estuary during the periodically stratified spring tide, and the dependence on the turbulence closure methods implemented in our SUNTANS simulations. This is in an effort to improve the predictions of the salinity front and the flow around the confluence and sill north of Jetty Island using the coarse grid (5 m around the study site) in preparation for simulation of surface coherent structures using the high-resolution grid (1 m around the study site). Via the generic length scale approach (Umlauf and Burchard 2003), we compared three two-equation closure schemes, namely k-kl, k- ϵ , k- ω , and two stability functions, namely KC (Kantha and Clayson 1994) and Canuto-A (Canuto et al. 2001), and found that the choice of stability function has a stronger effect than the choice of the turbulence closure scheme. Figure E1 depicts the predicted salt wedge profiles during the stratified weak tide along longitudinal transect E-E' (Figure E2). The simulation with the k-kl scheme and the KC stability functions predict notably stronger stratification and salt intrusion. The results from different closure schemes with the CA stability functions are similar, although the k- ω result appears to give slightly stronger mixing and thus weaker stratification. Nevertheless, the qualitative characteristics of turbulent mixing are robustly predicted in all the simulations.

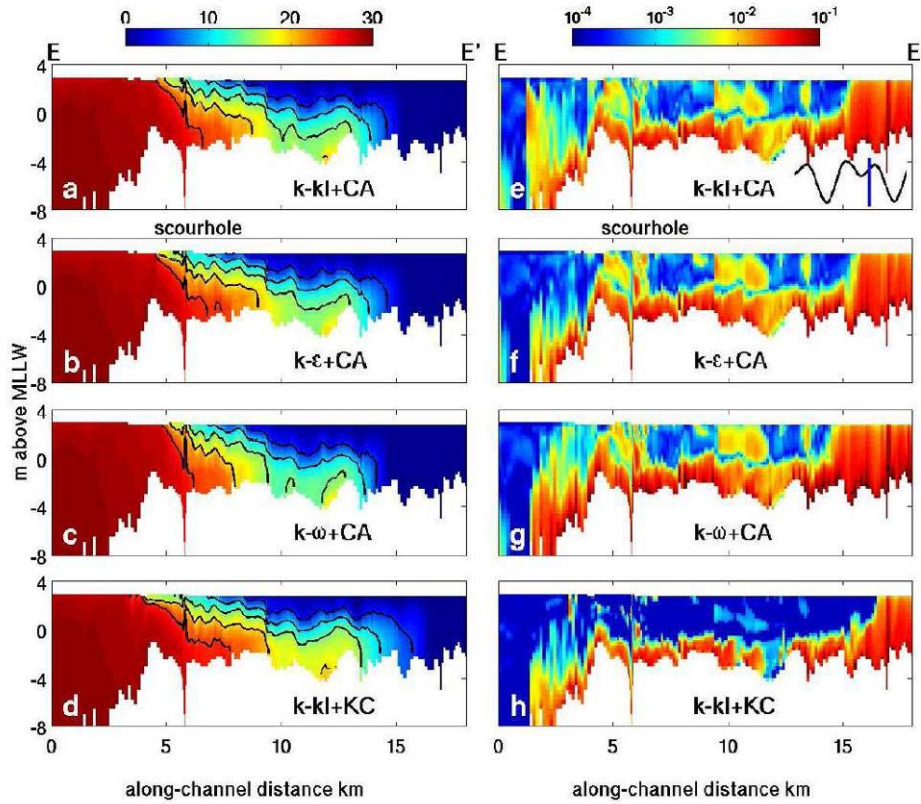


Figure E1: Salinity profile (left) and buoyancy flux (right) along transect E-E' during the weak flood from different combinations of turbulent closure schemes and stability functions. Tidal stage

is shown in plot e. The buoyancy flux, $- \rho_0 g \beta \frac{\partial s}{\partial z}$, is used here to indicate the strength of vertical mixing.

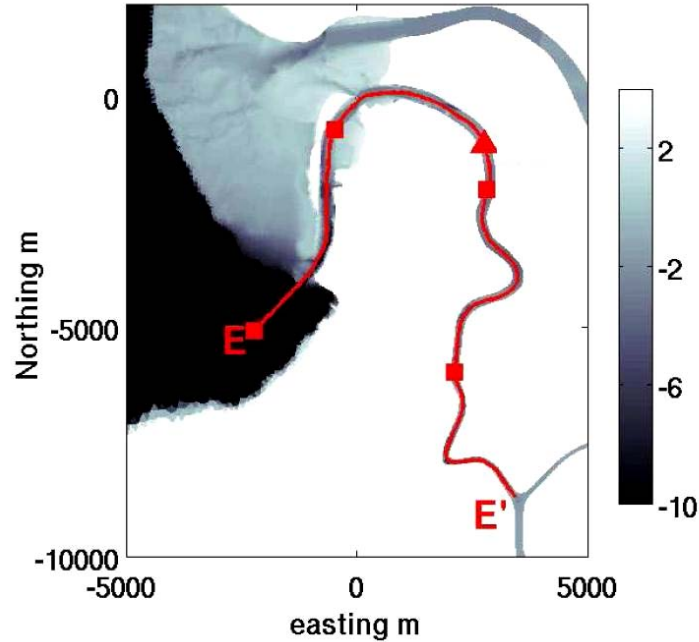


Figure E2: Location of transect E-E' plotted on top of bathymetry (m above MLLW). The squares are plotted every 5 km from point E.

Figure E3 illustrates the spatio-temporal evolution of the salinity field and turbulent mixing along transect E-E' at different stages of a tidal cycle. At low low water (Figure E3 a), the salinity front is advected to the mouth of the Snohomish River where relatively strong vertical mixing occurs. The strong flood advects the salinity front upstream by roughly 12 km and the vertical salinity structure is mostly maintained well-mixed by the strong flow except at the bypass confluence (Figure E3 b). During the subsequent weak ebb, stratification begins to develop due to baroclinic circulation and barotropic straining (Figure E3 c), and mixing occurs throughout the water column because the stratification is weak. The salt wedge (strong and stable stratification) is first established at the upstream portion of the salinity front where the horizontal salinity gradient is the greatest, and formation of the wedge gradually propagates downstream. The salt wedge appears at the study site at Jetty Island roughly during high low water (end of weak ebb) (Figure E3 d) and vertical mixing is confined along the density interface within the salt wedge at mid-depth. After the tide reverses to weak flood, a bottom-attached mixed layer grows due to destabilizing straining of the velocity profile, which effectively diminishes the stratification near the bottom (Figure E3 e). Overall, turbulent mixing has not significantly reduced the intensity of stratification in the estuary during the weak flood. Stratification persists until the middle stage of strong ebb, when the flow is sufficiently strong and the depth is shallow, at which time turbulent mixing is able to overcome the nonlinear effects of stratification. This, in turn, leads to an estuary-wide breakdown of the salt wedge.

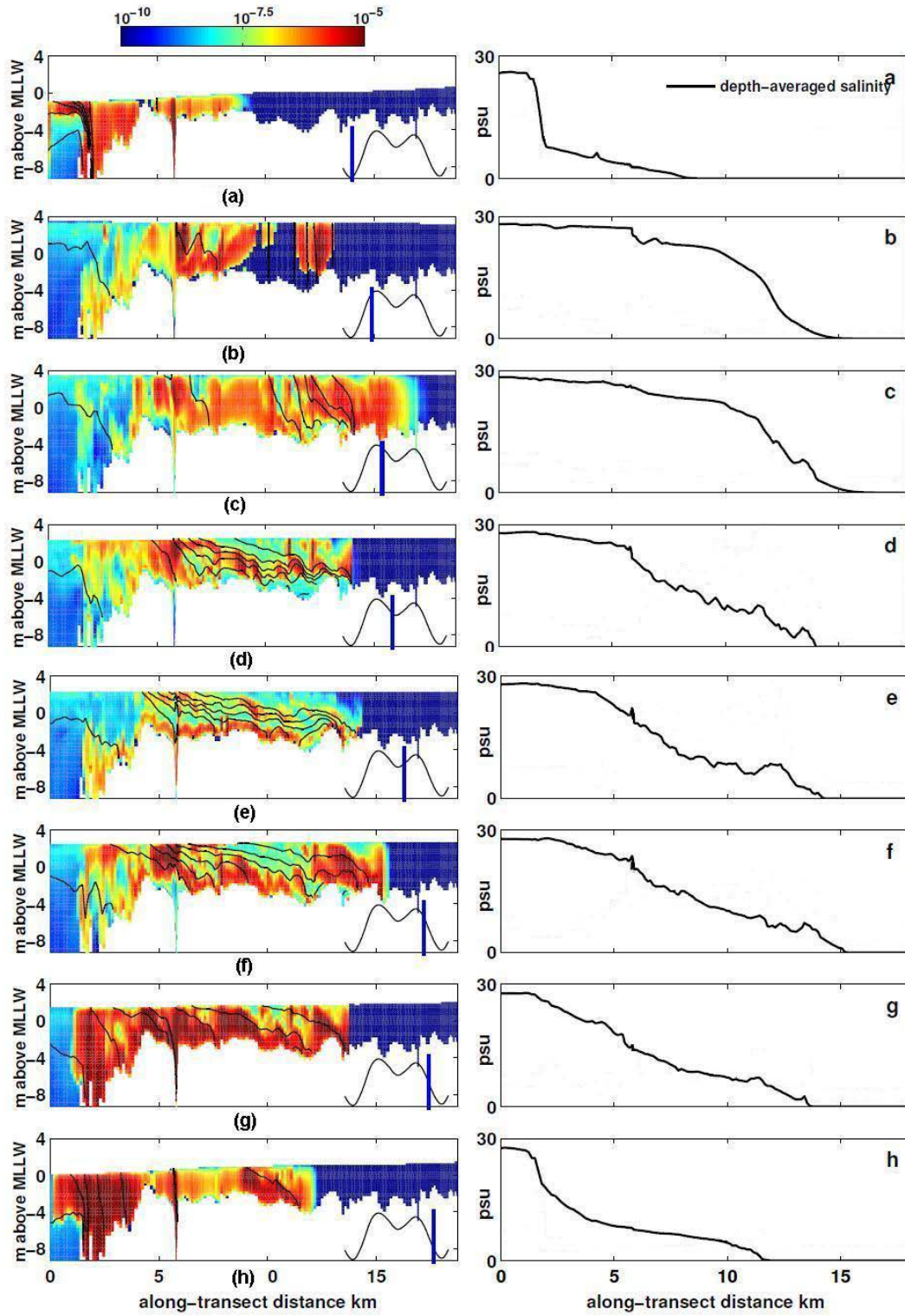


Figure E3: Buoyancy fluxes with salinity contours (left) and depth-averaged salinity along transect E-E' at different stages of a tidal cycle.

Idealized channel simulations with PCUI

The idealized simulations with PCUI over the idealized bathymetry depicted in Figure E4 were all performed with a fixed pressure gradient and bottom roughness. This allowed us to compute the form drag induced by the varying bed forms, since the streamwise velocity varied, which then caused the form drag coefficient to vary according to

$$C_F = -\frac{D}{\rho_0 U^2} p_x, \quad (1)$$

where D is the mean depth, U is the time- and space-averaged streamwise velocity, and p_x is the streamwise pressure gradient. An alternate measure of the drag coefficient can be obtained with (Fong et al. 2009) an estimate of the Reynolds stress as

$$C_S = -\beta \frac{\langle u'w' \rangle}{\langle u \rangle^2}, \quad (2)$$

where $\langle \rangle$ is the time-averaging operator and β is a fitting parameter that we employ because this expression is typically employed within the log-layer and we will employ it throughout the water column. Figure E5 compares equation (1) and (2) at mid-depth ($\beta=2.5$, triangles in the figure) and at the free surface ($\beta=160$, squares in the figure), and shows that agreement is remarkable, particularly for the results at the free surface. ***This implies that the bottom roughness can be inferred from estimates of the near-surface Reynolds stress and mean currents.***

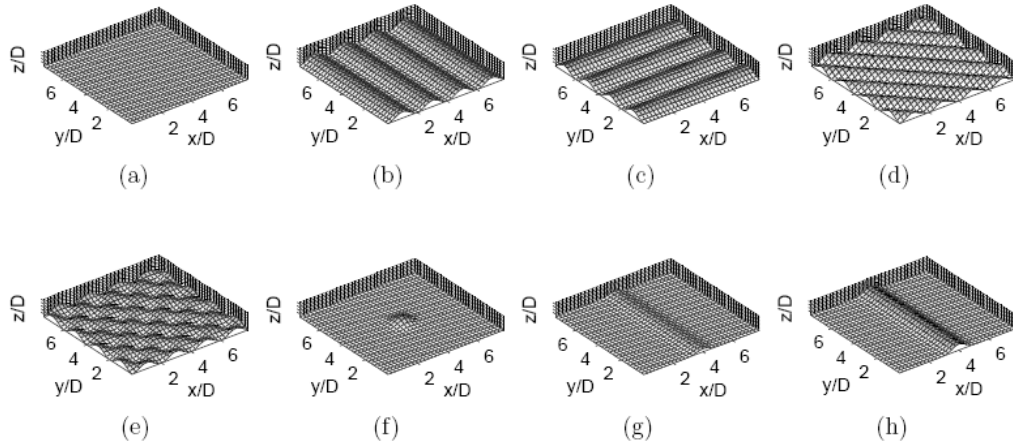


Figure E4: Bedforms investigated in the bedform study: (a) flat, (b) lateral, (c) longitudinal, (d) diagonal, (e) mixed, (f) 3D Gaussian, (g) short 2D Gaussian sill, and (h) tall 2D Gaussian sill. Mean flow is from lower left to upper right.

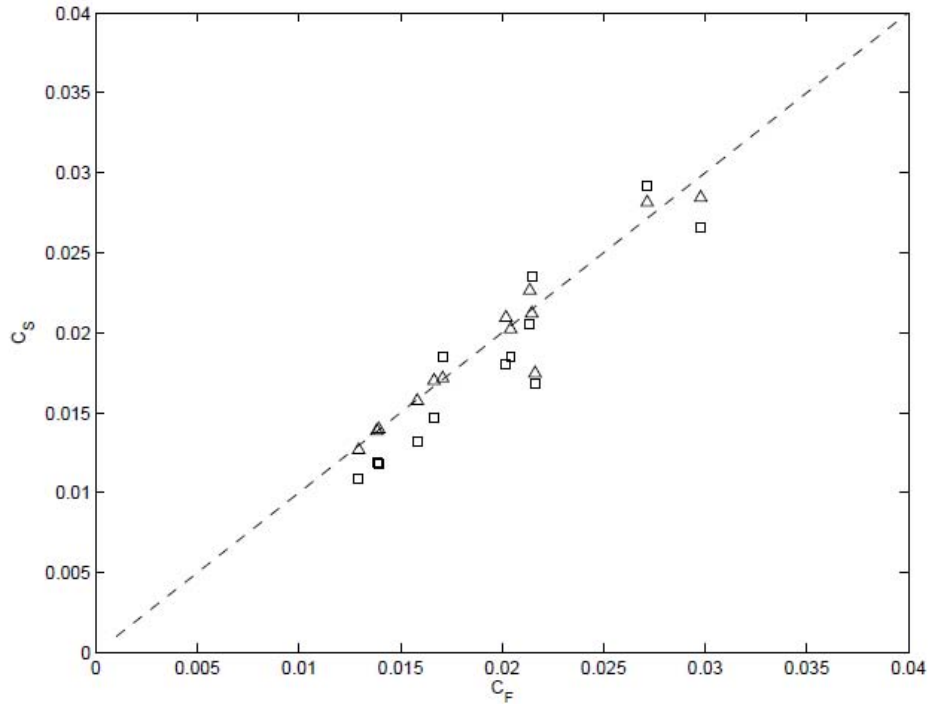


Figure E5: Comparison of the form drag coefficient computed with equation (1), C_F , to that computed with equation (2), C_S , at mid-depth (squares) and the free surface (triangles).

Using PCUI, we performed a simulation of a 200 by 80 m reach of the Snohomish River (site B) using high resolution multibeam bathymetry. In Figure E6 slices are colored by the downstream velocity, where red is fastest (0.7 m s^{-1}), and blue is no flow (or slight reversal). Data for this figure is from $t = 375\text{ s}$, and every-other cell from the computational grid is shown along the bed. This figure shows how turbulent the reach can be. Note that in the deeper pool the flow structures in the top-left portion of the figure are not impacting the free-surface as significantly as in shallower portions of the reach. A portion of the multibeam-based results is shown in Figure E7, where the visualization region is a subset of the reach, and the visualization region truncates the flow domain on all sides except the diagonal right side of the river. Flow is from the lower left to the upper right, and approximates the start of an ebb tide. Semi-opaque isosurfaces represent the vertical velocity, while the surface colors represent vertical velocity near the surface. The sequence of plots is a time series of upwelling evolution starting at slack, at 75-second intervals. The sequence shows that the vertical velocity forms mostly lateral coherent structures aligned with bed forms in the early stages of the flow. As the flow develops further it is clear that it becomes highly turbulent with vertical velocity flow structures that do not appear to contain any visible signature related to the bed forms. In the same simulation, a passive scalar was initialized with concentration given by the distance from the free-surface. Figure E8 presents the logarithm of the passive scalar plotted on the surface, where white indicates originally interior and bottom waters, and black indicates waters originating near the surface. Flow is from lower right to upper left for each panel. The upper left panel shows the bathymetric grid. The sequence shows that boils are first observed in shallower waters, and then spread across the entire free-surface as the flow accelerates. Figure E9 is of a similar situation, although the tracer is a thermal surface signature obtained from remote-sensing, and confirms the shallow to deep boil arrival sequence.

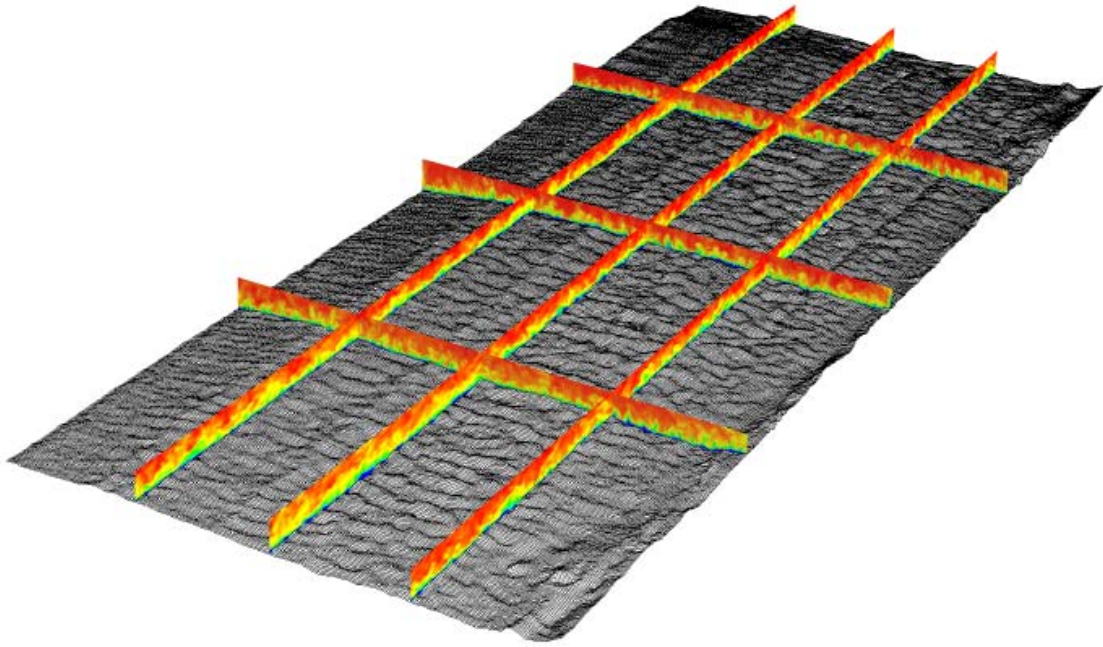


Figure E6: Slices of streamwise velocity over bathymetry derived from multibeam data, 375 s after slack water. Contours represent 0 (blue) to 0.7 m s^{-1} (red).

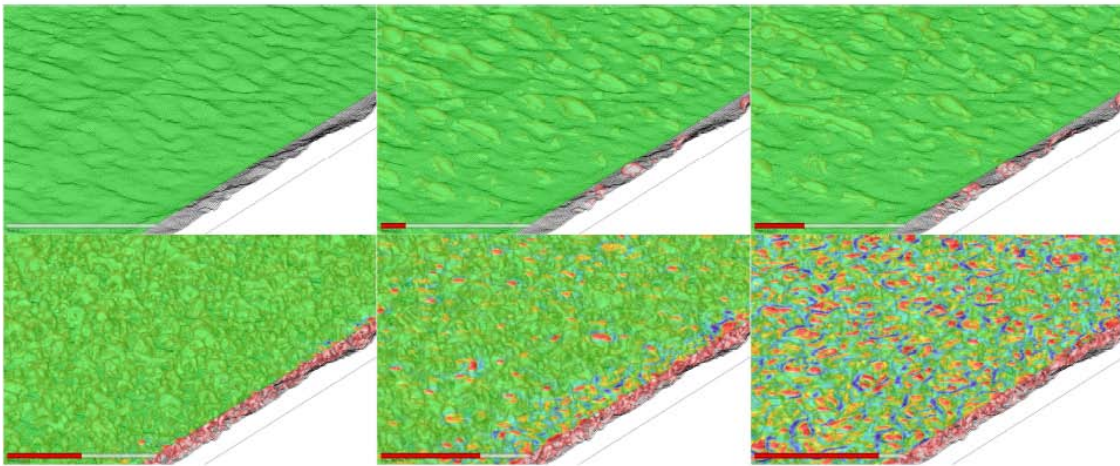


Figure E7: Time series of coherent flow structure evolution over real multibeam-based bathymetry. Semi-opaque isosurfaces represent the vertical velocity, while surface signature colors represent no upwelling (green), downwelling (blue), and upwelling (red).

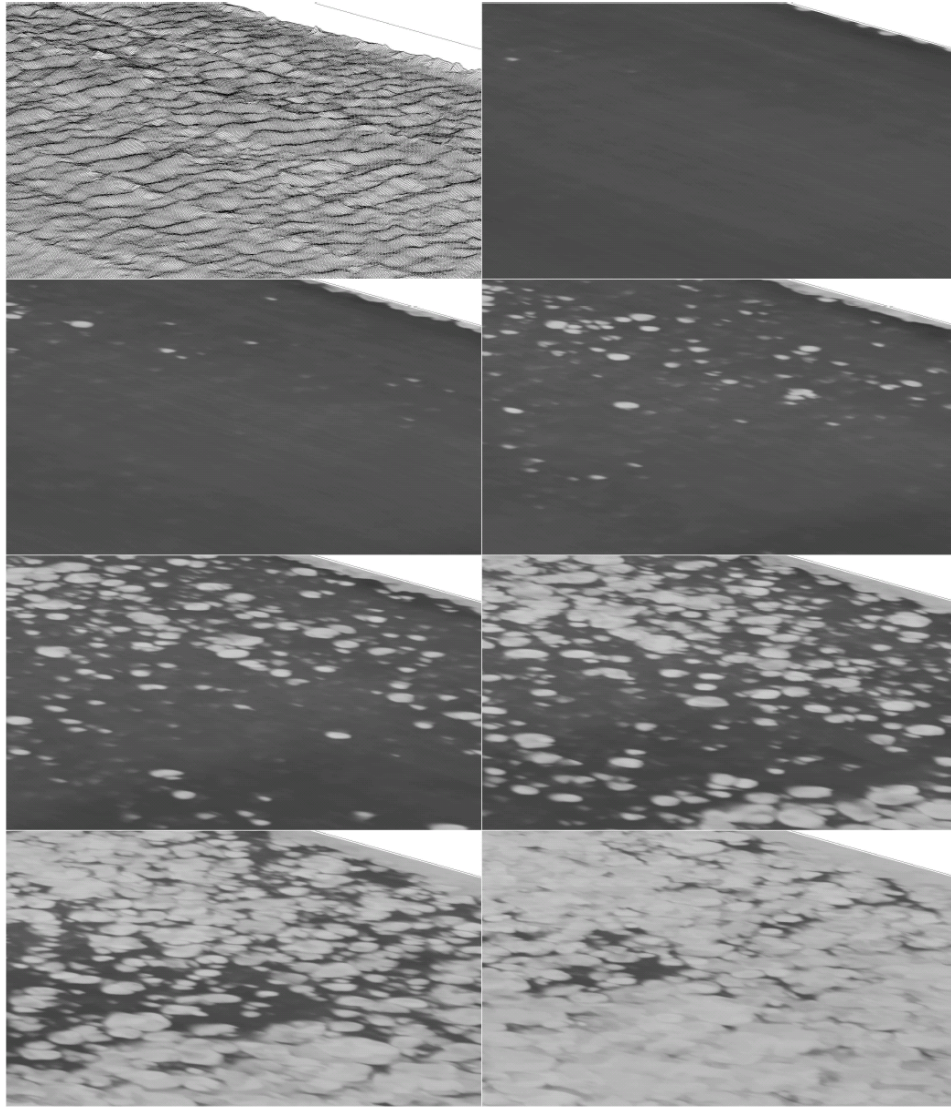


Figure E8: Time series of passive scalar signatures on the free-surface at 25 s intervals starting from $t = 225$ s (top right) to $t = 375$ s (bottom right) after slack water.

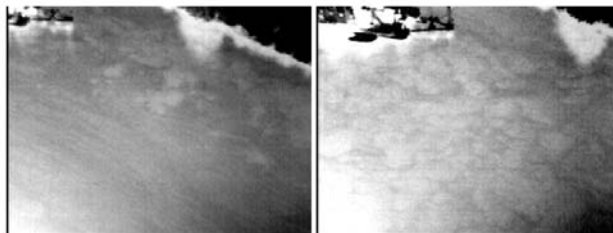


Figure E9: Infrared images of surface boils in a tidal river, near slack (left), and 28 minutes later (right). Flow is from lower right to upper left. A research vessel is visible in the upper left corner, and the thermal reflection of a tree can be seen at the edge of the bank which runs diagonally across the upper right.

F: Microwave Remote Sensing

Radar measurements during COHSTREX 2009 were made using a bankside, X-band coherent radar and three different airborne synthetic aperture radars (SARs).

The X-band Doppler radar, RiverRad, was deployed in the bed of a pick-up truck beside the Snohomish River during the time that measurements on the APL barge were being made. Data were collected continuously, day and night, from 17:00 PDT on September 9, 2009 to 10:09 PDT on September 25, 2009. The only exceptions were when the radar was being repositioned after the barge had moved. Figure F1 shows the radar in operation with the barge in the background. RiverRad's two antennas were operated with azimuth angles 20° apart. Both were VV polarized. A video camera was aligned with the mean azimuth angle of the antenna and recorded an image of the field viewed by the radar every 30 seconds.

Preliminary results from the RiverRad measurements are shown in Figure F2. The radar data are shown overlaid on an optical GeoTiff image in all but the upper right panel. That panel shows the tidal height on the river and the time of the measurement as the red circle. The goal of the radar measurement was to measure surface roughness and velocity as a function of tidal phase. The upper right panel shows velocity vectors obtained from the combination of the Doppler shifts to the two antennas. The bottom row shows the received power (left) and radial currents (right) observed by the two radar antennas. A scour hole was located near the east bank of the river just north of the radar and evidence can be seen of increased surface roughness and velocity near the hole.

To study microwave signatures of coherent structures on rivers using airborne radar, we collaborated with David Long at Brigham Young University and Artemis, Inc. (<http://www.artemisinc.net>) to field small synthetic aperture radar systems (micro SARs) during the 2009 field campaign. The BYU microSAR is a low-cost low-power synthetic aperture radar that is capable of imaging an area with a resolution of 1.875 meters. The Artemis microASAR system is a commercial derivative of the BYU microSAR, and is capable of imaging scenes with a resolution of 0.75 meters. Artemis also tested their development system (the SlimSAR) which consists of L- and X-band SARs.

The three airborne synthetic aperture radars (the BYU microSAR, the Artemis microASAR, and the Artemis SlimSAR) were used to image the Snohomish River during the COHSTREX 09 field campaign. The microASAR and the SlimSAR, made measurements on September 10 and September 12. Figure F3 shows an image from the L-band channel of the SlimSAR system superimposed on Google Earth imagery. The image has a pixel size of 0.5 m x 0.5 m. The inherent resolution of the system in the range dimension is 1.8 m, and in the azimuth direction is around 10 cm. The APL barge (the Henderson) is the brightest feature on river. On the either side of the river, clear images of the farm land and man-made structures are visible. Two patches of increases backscatter from the river, one north of the barge, and the other south of the barge, up-river of the sharp bend, can be seen in image. We still need to process more of this data to determine whether these features are due to surface roughness on the river, or an imaging artifact. We also have co-registered C-band imagery from the microASAR system, but further processing is needed to remove imaging artifacts caused by radar return measured through the sidelobes of the antenna.



Figure F1. RiverRad, a X-band coherent radar, deployed in a pickup truck along the river bank.

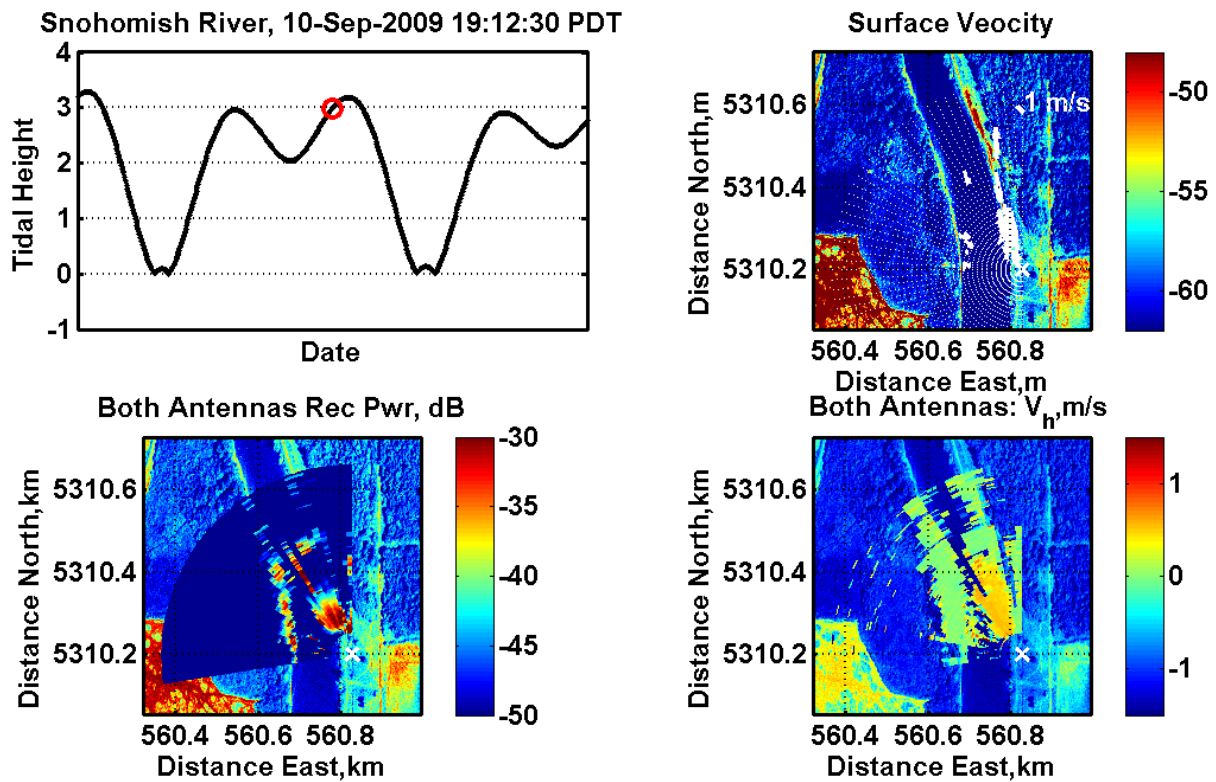


Figure F2. Example results from RiverRad. Clockwise from top left: Tide timeseries, surface velocity map, radial currents map, received power map.



Figure F3. L-band micro SAR image of the Snohomish River superimposed on Google Earth imagery. The SAR image covers 2.3 km in the cross track direction, and 4.9 km in the along track direction. The brightest feature on the river is the APL barge (the Henderson). Farmland and man-made features are clearly visible on either side of the river.

The BYU microSAR was flown on six different occasions during the project to sample different phases of the tide. This system was flown on a Cessna 172 operated by a local company. The antennas for the radar were mounted to the belly of the plane and enclosed in an aerodynamic radome. Figure F4 shows the microSAR antennas mounted to the aircraft (the radome has been removed in this picture). The electronics for the radar were strapped down on the back seat of the aircraft. An infrared camera was also mounted to the aircraft, providing us with airborne infrared measurements for the same periods as the microSAR measurements. Initial analysis of the microSAR data shows significant interference from ground-based wireless network signals. However, we are confident that this interference can be removed with further processing.



Figure F4. microSAR antennas mounted to the belly of the Cessna 172 aircraft. The incidence angle of the antennas is adjustable. A fiber glass aerodynamic radome (not shown) covers the antennas in flight.

IMPACT/APPLICATIONS

Our results demonstrate how currently available prediction schemes and observing systems (remote sensing and AUVs) can be combined for operational applications.

RELATED PROJECTS

Airborne IR/EO measurement system used for the COHSTREX 09 Experiment was developed for Tidal Flats DRI.

REFERENCES

- Fong, D.A., Monismith, S.G., Stacey, M.T., and J.R. Burau, 2009, Turbulent stresses and secondary currents in a tidally-forced channel with significant curvature and asymmetric bed forms. *Journal of Hydraulic Engineering*, 135 (3), 198-208.
- Umaluf, L. and H. Burchard, 2005: A generic length-scale equation for geophysical turbulence models. *Journal of Marine Research*, 61, 235-265.
- Kantha, L. H. and C. A. Clayson, 1994: An improved mixed layer model for geophysical applications. *Journal of Geophysical Research*, 99, 25,235-25,266.

Canuto, V. M., A. Howard, Y. Cheng, and M. S. Dubovikov, 2001: Ocean turbulence I: one-point closure model--Momentum and heat vertical diffusivities. *Journal of Physical Oceanography*, 31, 1413-1426.

PUBLICATIONS

Barad, M. F., and O. B. Fringer, 2009, "Identifying bedforms from free-surface observations: A numerical study", *J. Hydr. Eng.*, submitted [refereed].

Chickadel C. C., A. R. Horner-Devine, S. A. Talke, A. T. Jessup (2009), Vertical boil propagation from a submerged estuarine sill, *Geophys. Res. Lett.*, 36, L10601, doi:10.1029/2009GL037278 [published, refereed].

Giddings, S. N., D. A. Fong, S. G. Monismith, C. C. Chickadel, K. A. Edwards, W. J. Plant, A. R. Horner-Devine, A. T. Jessup, 2009, Comparative analysis of simultaneous in-situ and remote sensing observations of a persistent front in a shallow macrotidal estuary, *Limnol. Oceanogr. :Methods*, submitted [refereed].

Plant, W.J., R. Branch, G. Chatham, C.C. Chickadel, K. Hayes, B. Hayworth, A. Horner-Devine, A. Jessup, D.A. Fong, O.B. Fringer, S.N. Giddings, S.Monismith, B. Wang, 2009, Remotely Sensed River Surface Features Compared with Modeling and In-Situ Measurements, *J. Geophys. Res.*, to appear [in press, refereed].

Talke, S.A., A.R. Horner-Devine, 2009. Mixing layer dynamics in separated flow over an estuarine sill with variable stratification, *J. Geophys. Res.*, to appear [in press, refereed].

Wang, B. , O. B. Fringer, S. N. Giddings, and D. A. Fong, 2009, "High-resolution simulations of a macrotidal estuary using SUNTANS", *Ocean Modelling*, 26 (1-2), 60-85, doi:10.1016/j.ocemod.2008.08.006 [published, refereed].